ORIGINAL ARTICLE

A modified volumetric energy density–based approach for porosity assessment in additive manufacturing process design

Paolo Ferro[1] · Roberto Meneghello[1] · Gianpaolo Savio[2] · Filippo Berto[3]

Abstract

Soundness of additively manufactured parts depends on a lot of process and geometrical parameters. A wrong process design leads to defects such as lack of fusion or keyhole porosity that have a detrimental effect on the mechanical properties of the printed parts. Process parameter optimization is thus a formidable challenge that requires in general a huge amount of experimental data. Among the others, heat source power and scan speed are the most defects-affecting parameters to be optimized. The energy density is used in literature to quantify their combination. Unfortunately, in different works it was demonstrated that it fails if used as design parameter mainly because it does not take into account the material properties and the interaction between heat source and the powder bed. In this contribution, a modified volumetric energy density equation that takes into account the powder-heat source interaction to optimize the combination of power-scan speed values for porosity assessment in powder bed fusion process design is proposed and verified on both AlSi10Mg alloy and Maraging steel 300.

Keywords Additive manufacturing · Aluminium alloy · Maraging steel · Selective Laser Melting · Porosity · Energy density

1 Introduction

Additive manufacturing (AM) processes are attracting the attention of both industry and academic world, thanks to the great potential they can provide. When compared with traditional manufacturing processes the key advantages are (i) high degree of design freedom, (ii) easy change or revision of a product, (iii) reduction of waste production and energy costs, and (v) with reference to powder bed fusion (PBF) processes applied to metallic materials, mechanical properties of the as-build components are often equal, or even greater than those of the same parts obtained with standard subtractive methods or casting processes [1]. However, there are still some issues to be faced in order to make AM processes more and more usable for

industrial applications. When applied to metallic materials, because of the rapid melt pool solidification, few alloys are at the moment suitable and available in the market for additive manufacturing. The new microstructures arising from rapid alloy solidification require a new characterization of the material and last but not least, the numerous parameters affecting the soundness of the additively manufactured components force the manufactures to a formidable parameters' calibration.

The complex interaction between the heat source and the powder layer, as well as the complex thermal phenomena that occur during the printing process, may result in different kinds of defects such as pin hole voids, incomplete melting, or incomplete filling. Gas pores, for example, may arise from powder surface chemistry modification and/or trapped gas in

✉ Paolo Ferro
  paolo.ferro@unipd.it

  Roberto Meneghello
  roberto.meneghello@unipd.it

  Gianpaolo Savio
  gianpaolo.savio@unipd.it

  Filippo Berto
  filippo.berto@ntnu.no

[1] Department of Engineering and Management, University of Padova, Stradella San Nicola 3, 36100 Vicenza, Italy

[2] Department of Civil, Environmental and Architectural Engineering, University of Padova, via Venezia 1, 35131 Padova, Italy

[3] Department of Engineering Design and Materials, NTNU, Richard Birkelands vei 2b, 7491 Trondheim, Norway

particles that are released during melting and locked in during solidification. But they may also be due to key-hole effect for deep melt pools. Elongated pores are process-induced defects and are due to an inefficient melting regime or spatter and fumes ejection [2]. The geometry of the part plays an important role in the fabrication process, as well. Every change in the geometry will change the way the AM machine performs its fabrication routine affecting the properties of the resulting solid [3, 4]. One way to study the interaction between final part properties and processing parameters is to carry out different 'trial and error' experimental tests. A second possibility is the in situ monitoring and in-line quality control of the process itself [5–8]. However, they are still challenging to implement in actual machines for industrial production. Finally, numerical simulation can be used as a powerful tool to support experiments by reducing the number of tests necessary for process parameter optimization [9, 10]. A great consensus is there in literature in considering the energy density as one of the best predictors for parts relative density for powder bed fusion (PBF) processes. There are different formulations of such parameter. The volumetric energy density (VED) is used above all to describe the experimental data coming from laser powder bed (LBP) tests [11–16]. and it is formulated starting from the most important process parameters as follows [17]:

$$E_d = \frac{P}{v\,h\,d} \tag{1}$$

where P is the laser power, v is the scan speed, h is the hatch distance, and d is the layer thickness. Despite the intensive use of the VED in literature, many criticisms have been made about its real effectiveness as a design parameter [18]. As a matter of fact, Eq. (1) may not properly represent the effective energy transferred to melt the powder bed, and thus, it should be improved involving the material properties. It is suggested that the melted volume does not correspond exactly with the parallelepiped defined by VED, but that melted volume will scale fairly linearly with the volume of this parallelepiped for successful recipes [19, 20]. Bertoli et al. [21] outlined in their work the suitability of VED as a design parameter to describe selective laser melting (SLM), but at the same time, they encourage to be careful in using it because its incapability to capture the complex physics of the melt pool.

Willy et al. [22] proposed a modification of Eq. (1). In effect, for fixed values of h and d, the laser power (P) is proportional to the scanning speed (v): $P = k \cdot v$ (with $k =$ constant). This means that for a static laser ($v = 0$), a molten pool would be obtained even without laser ($P = 0$), which has no physical significance. The relationship was thus modified by introducing an 'off-set power' P_0: $P = P_0 + k \cdot v$. However, the modified relationship was verified to be true only for a limited range of laser power. Despite such criticism against

the use of VED as design parameter, it continues to be proposed in different works [15, 23–25]. In a recent work, Caiazzo et al. [26] studied the relevance of VED in the investigation of Inconel 718 LPBF. They proved how different technological and mechanical properties of additively manufacturing parts such as roughness, hardness, number, and size of pores as well as fractional density can be explained in terms of VED that can help the designer in dealing with several process parameters as once.

One of the main goals in AM process parameter optimization is to understand how they interact with the powder bed. Dimension and shape of fusion zone as well as defects are the main characteristic to be predicted as a function of process parameters. In this scenario Hann et al. [27] considered the mean surface enthalpy to compute the melt depth and width for different materials, predicting the transition from melting to keyholing and porosity in welding. They started from the empirical observation that the shape of a weld is a function of the 'enthalpy' of the material (specific energy per unit kilogram) and found the basic thermodynamic arguments to identify the origin of it. This result was confirmed by Metelkova et al. [28] that used both the VED approach and the normalized enthalpy to link the melt pool morphology with the heat input in SLM process. They showed how the VED parameter (Eq. 1) was unsuitable to predict the melt pool depth especially at high energy input. On the other hand, the normalized enthalpy was found to work.

The utility of using the normalized enthalpy to combine the effects of power, speed, and beam size was also validated experimentally by King et al. [29]. They found that the normalized enthalpy can be used to identify the keyhole threshold from experiments but appears to be missing some physics particularly with regard to the dependence of melt pool depth on beam size in the conduction mode. Correlations between the melt pool aspect ratio and the process parameters were also found by using both the normalized enthalpy and VED [30]. Single bead experiments were carried out for high deposition rates identifying the thresholds of the process parameters resulting in voids [30]. The aspect ratios (ARs) versus the normalized enthalpy correlations showed much less scattered data as opposed to the AR versus VED plot. This is because, as in previous works, the normalized enthalpy takes into account the interaction between the material and the laser parameters, while the VED, in actual formulation (Eq. 1), does not.

This is the main reason why a new mathematical expression of such parameter (VED) is proposed in this work that overcomes the major drawback of the original formulation, i.e., the heat source-powder interaction phenomena. While the original definition of VED was found incapable to capture the optimal process parameters that maximize the fractional density, the proposed definition of VED allowed to define a narrow range of energy density values that minimize samples

Table 1 Chemical composition of the alloy AlSi10Mg (wt%)

Al	Si	Mg	Fe	N	O	Ti	Zn	Mn	Ni	Cu	Pb	Sn
Balance	9–11	0.25–0.45	< 0.25	< 0.2	< 0.2	< 0.15	< 0.10	< 0.10	< 0.05	< 0.05	< 0.02	< 0.02

porosity. In this way it is possible to predict the porosity as a function of materials and process parameters, in different melting condition such as keyhole mode and conduction mode, by using a single VED model integrating thermal and physical properties.

2 Materials and Methods

The analysed material is the AlSi10Mg hypoeutectic alloy, mostly used for aluminium castings. Its chemical composition is collected in Table 1. The little amount of Mg (0.3–0.5 wt%) allows the reinforcement by natural or artificial ageing, while its near eutectic composition (Fig. 1) enhances its castability.

The particle size of the AlSi10Mg powder is in the range of 15–45 μm. The samples were manufactured by selective laser melting Renishaw AM 400, which is equipped with a 400-W pulsed ytterbium fibre laser with a wavelength of 1.070 μm and a 70-μm spot size at the focus plane (Φ). The building square-based platform has a side length equal to 250 mm. Argon was used as protective gas against powder oxidation. Cylindrical specimens were produced with diameter and length equal to 10 mm (Fig. 2).

In order to reduce the possible process parameters combinations, the following inputs were kept constant during the tests:

- Layer thickness (d), 30 μm
- Platform temperature, 170 °C
- Point distance (s) equal to hatch distance (h), 80 μm

- Building direction: sample axis

In Fig. 3 the laser scanning strategy and the definition of point distance and hatch distance are shown.

With the aim to minimize the porosity inside the material, the laser beam power (P) and exposure time (t_e) values were changed starting from those suggested by Renishaw (say, 275 W and 40 μs, respectively). Values of P and t_e used in the experiments are collected in Appendix (Table 2). Three cylindrical samples for each couple of process parameters were carried out.

It is noted that even if it was not possible to change the scan speed (v), this last parameter can be approximated with the following relation:

$$v \approx \frac{s}{t_e} \qquad (2)$$

Samples for microstructural analyses were embedded in phenolic resin and prepared using standard grinding and polishing procedures. In particular, grinding was employed by using only one SiC abrasive size (P400) with the surface water-cooled and the platen rotated at about 240–280 rpm. Polishing was carried out using a diamond abrasive size followed by final polishing with colloidal silica. The microstructure was analysed using a scanning electron microscope (Quanta 2580 FEG, FEI, Boston, MA, USA). Light microscopy pictures were also taken with Leica DMC 2900 microscope. With the help of a dedicated software for image analysis, the microscope is driven to obtain the overall specimen image by means of the combinations of several micrographs carried out by scanning the entire surface of the specimen. The

Fig. 1 Aluminium–silicon phase diagram
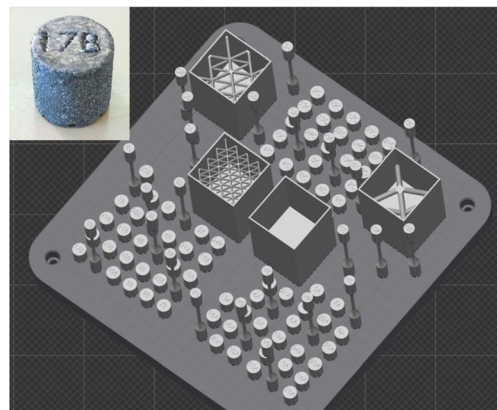
Fig. 2 Geometry of the specimens and their position on the building platform

Fig. 3 Scanning strategy (**a**); spot-to-spot fabrication process, where 's' is the point distance, 'Φ' is the laser beam spot and h is the hatch distance (**b**)
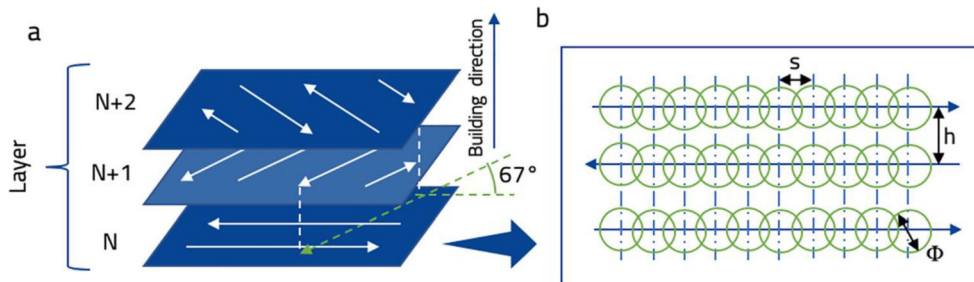
final micrograph is then processed for the automatic counting of the area interested by porosity. Figure 4 shows the result of the micrographs processing routine above described for two cylindrical samples.

3 Energy density formulation

One of the main criticisms made against the definition of VED (Eq. (1)) is that the melting of multiple layers and the keyhole shape of the melt pool often invalidates the use of the layer thickness (d) as the depth parameter used to calculate the volume affected by the source energy [31]. This last parameter can be extimated by the one-dimensional model describing the temperature distribution (T) along the source axis direction (z) [32, 33]:

$$T(z,\tau) = \frac{P\beta}{Ak}\sqrt{4\alpha t_e}\,ierfc\left[\frac{z}{\sqrt{4\alpha\tau}}\right] \tag{3}$$

In Eq. (3), A is the spot area, k is the thermal conductivity, α is the thermal diffusivity, β is the absorption factor, z is the distance from surface, τ is interaction time, and ierfc stands for 'integral of the complimentary error function' given by the following equation:

$$ierfc(u) = \frac{e^{-u^2}}{\sqrt{\pi}} - u[1 - erf(u)] \tag{4}$$

with erf(u) as the error function. The heat source penetration

(H) is obtained when the limit of Eq. (3) approaches zero. This happens when $z = H = \sqrt{4\alpha\tau}$. While 90% of temperature change occurs within 1 scaling parameter of surface [30], the interaction time (τ) can be expressed by Φ/v where Φ is the spot size diameter [34]. Therefore, by taking into account the absorptivity and the penetration of the heat source (Fig. 5), Eq. (1) can be rewritten as follows:

$$E_{d,\text{eff}} = \frac{\beta P}{v \cdot h \cdot \sqrt{4\alpha\dfrac{\Phi}{v}}} = \frac{\beta}{h\sqrt{4\alpha\Phi}}\frac{P}{\sqrt{v}} = C\frac{P}{\sqrt{v}} \tag{5}$$

For pulsed laser powder bed fusion processes, by taking advantage of Eq. (2), Eq. (5) can be written as

$$E_{d,\text{eff}} = \frac{\beta}{h\sqrt{4\alpha\Phi s}}P\sqrt{t_e} = C_1 P\sqrt{t_e} \tag{6}$$

It is observed that compared with the previous energy density formulation used in literature (Eq. (1)), Eq. (5) takes into account both the material-laser interaction through the parameter β, and the material properties via the powder thermal diffusivity α.

The constant C in Eq. (5) (or C_1 in Eq. (6)) needs to be calculated starting from material properties as well as the absorptivity value (β) that can be estimated by experiments or numerical simulation. It has to note that the absorptivity may vary with the combination of heat source powers (P) and scanning speeds (v) since such parameters influence the

Fig. 4 Processed images for the porosity amount assessment (samples obtained with: **a** power = 375 W, exposure time = 30 μs; **b** power = 300 W, exposure time = 30 μs)
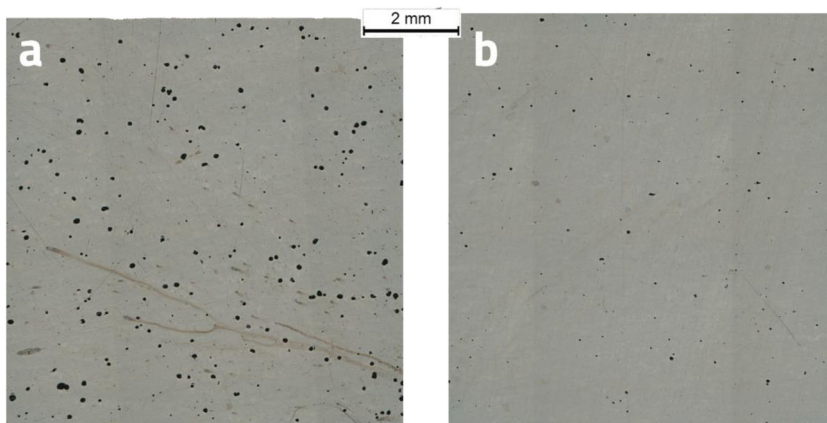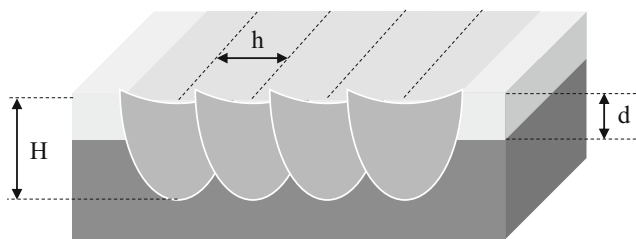
Fig. 5 Schematic of volumes effectively affected by the heat source (with H = heated depth)

depression induced by the recoil pressure on the melt pool and thus the heat absorption [35, 36]. However, this phenomenon would complicate the use of the $E_{d,eff}$ as design parameter; therefore, in this work, it is ignored and the value of β as well as α are kept constant. It is worth mentioning that α should be calculated starting from the effective powder properties as defined for instance by Ning et al. [37]:

$$\rho_e = (1-\varphi)^\gamma \rho_s \qquad (7)$$

$$k_e = (1-\varphi)^\eta k_s \qquad (8)$$

where ρ is the density; subscripts e and s stays for effective and solid, respectively; while γ and η are coefficients that can be taken equal to 1 and φ is the porosity (say, 0.4) [38].

However, it is observed from Eqs. (7) and (8) that the same reduction was attributed to the density and thermal conductivity of the powder compared with those of the consolidated material. Therefore, because even the specific heat of the powder does not change significantly compared with that of the bulk material, the powder diffusivity can be approximated to that of the consolidated material. Figure 6 shows the iso-VED curves as well as two of their derivatives obtained both with

the original and actual formulation (Eq. (1) and Eq. (6)). It is observed that the difference in curve shape is attributed to the different dependence of the power with the scan speed (or exposure time), say the inverse of scan speed (Eq. 1) against the inverse of the square root of scan speed (Eq. 5). It is also noted that such difference (highlighted by the derivatives) is more pronounced as the scan speed increases, or the exposure time decreases, therefore in the more interesting part of the diagram for industrial applications.

4 Results and discussion

4.1 Microstructure

According to process parameters, pores or lack of fusions (LoF) are easily formed during the SLM process. Figure 7 shows some pores and LoF defects detected in the present experimental work. According to the phase diagram (Fig. 1) the microstructure (Fig. 7c) is characterized by α-Al dendrites inside a eutectic matrix constituted by α-Al and nanometric Si-particles.

Figure 8 shows some micrographs taken from cylindrical samples obtained by varying both the laser power (P) and the exposure time (t_e). Only some particular combinations of power and exposure time allow to obtain sound samples. As suggested in literature, it is supposed that such positive parameter combinations are linked by the same value of VED. For the sake of simplicity, Figure 8 collects only some significative micrographs as a function of a limited range of process parameters tested. On the other hand, the mean value of the area percentage occupied by pores as a function of the entire range of tested process parameters is shown in Fig. 9, where

**Fig. 6** Iso-energy density curves and their derivatives
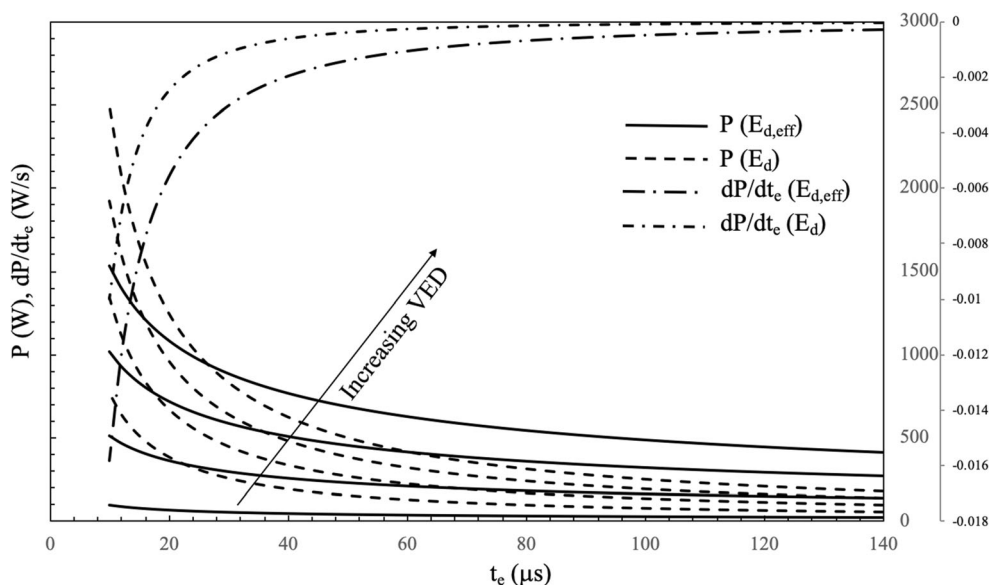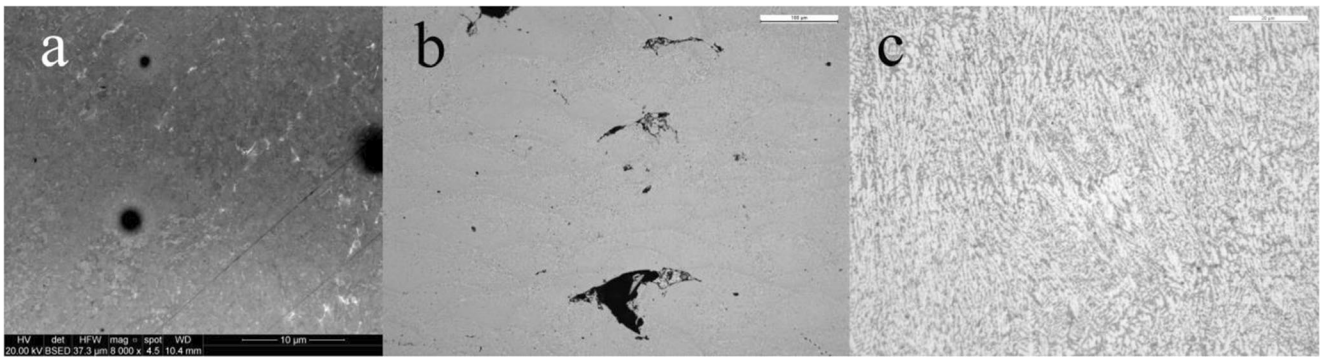
Fig. 7 Porosity (**a**), lack of fusion (**b**), and microstructure observed in AlSi10Mg samples

the bubble areas are proportional to the porosity percentage detected in the cylindrical samples.

In Fig. 9 two iso-volumetric energy density curves calculated using Eq. (6) are plotted, as well. According to literature [39, 40] the absorptivity and the thermal diffusivity are taken equal to 0.18 and $5.7 \cdot 10^{-5}$ m^2/s, respectively; therefore, the constant C_1 in Eq. (6) results to be 2 s$^{1/2}$/mm^3. It is worth mentioning that different absorptivity values can be found in literature depending on material, particle dimensions, models, and other processing conditions [35, 41, 42].

It is interesting to point out that despite the high reflectivity of aluminium alloys, the absorptivity of its powder is higher than that of the consolidate material, thanks to the multiple reflections and absorptions of the rays that strike the powder particles [43]. Almost all the P/t_e combinations that assure a porosity less than 1% stay in between the two iso-VED curves, $E^s_{d,\text{edff}} = 4.2$ J/mm^3 and $E^i_{d,\text{edff}} = 3.2$ J/mm^3 plotted in Fig. 9. This validates the proposed VED as design parameter. On the other hand, it is easy to observe that it is not possible to interpolate the process parameters combination (P, t_s) assuring a porosity
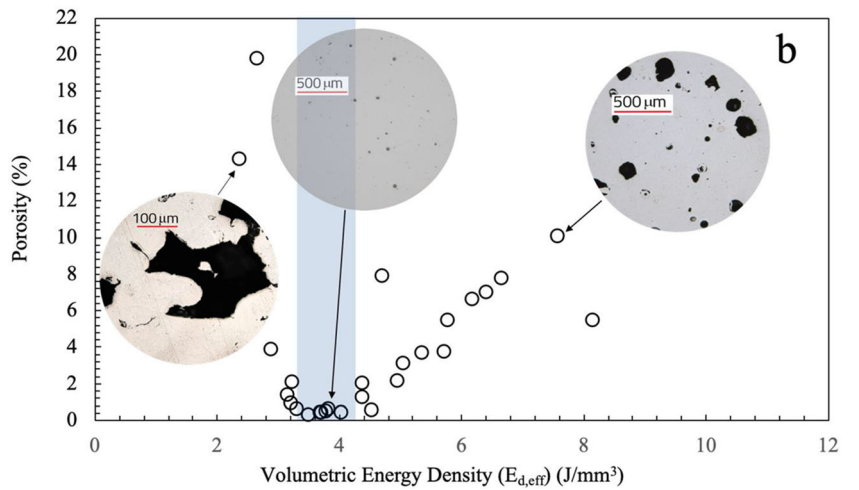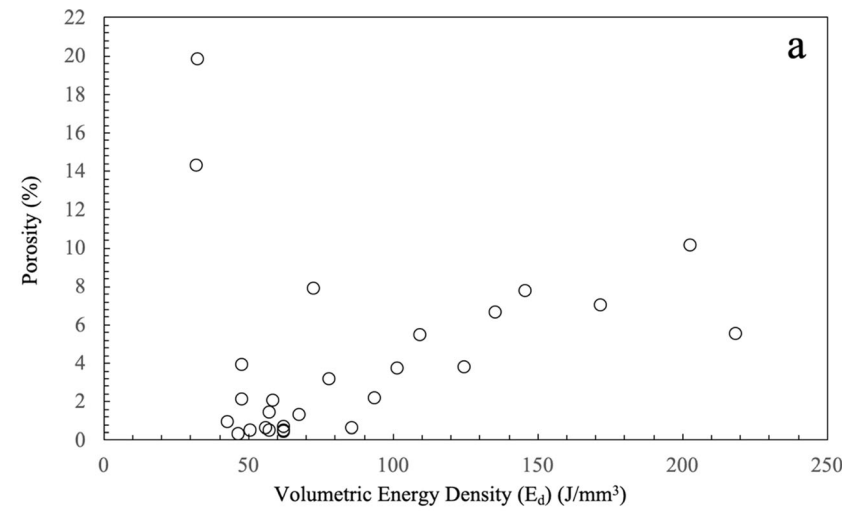
Fig. 8 Some micrographs (magnifications × 50) showing porosity as a function of laser power (*P*) and exposure time (*t_e*)
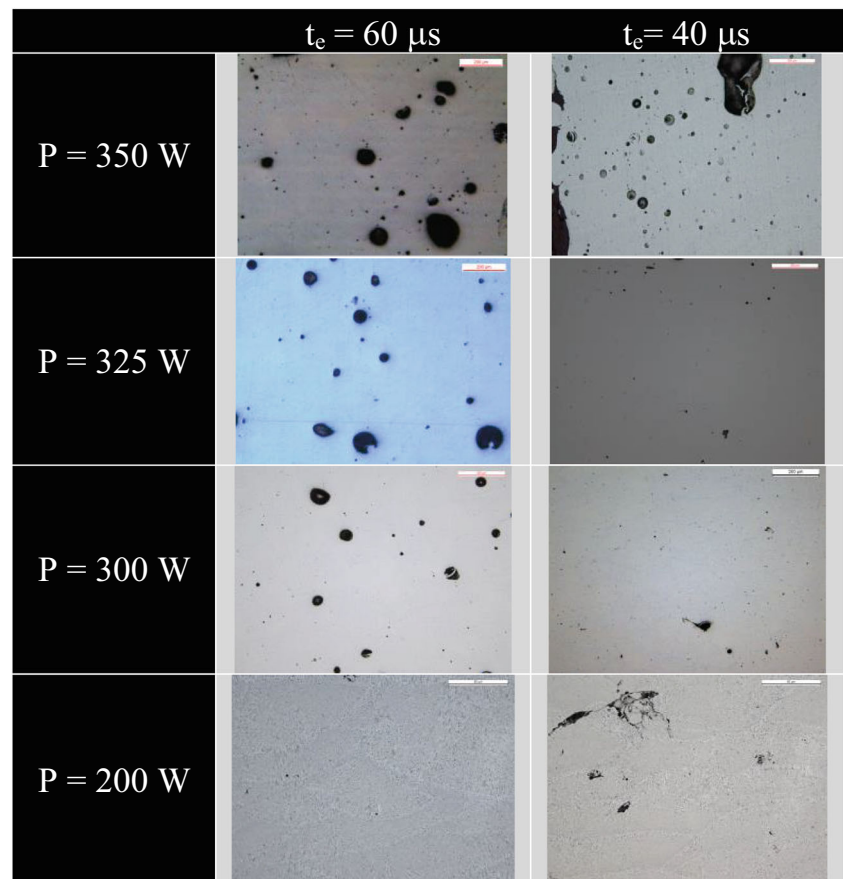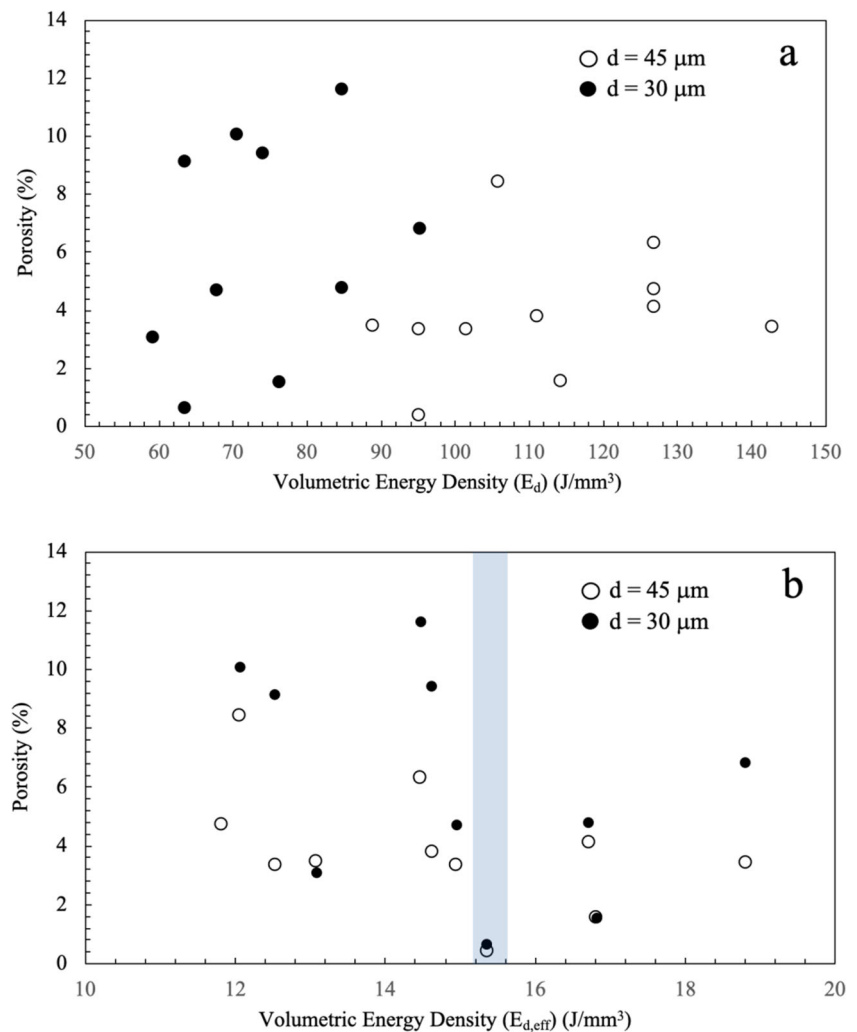
Fig. 9 Porosity percentage (%) as a function of process parameters (laser power, exposure time) and energy density ($E_{d,eff}$)
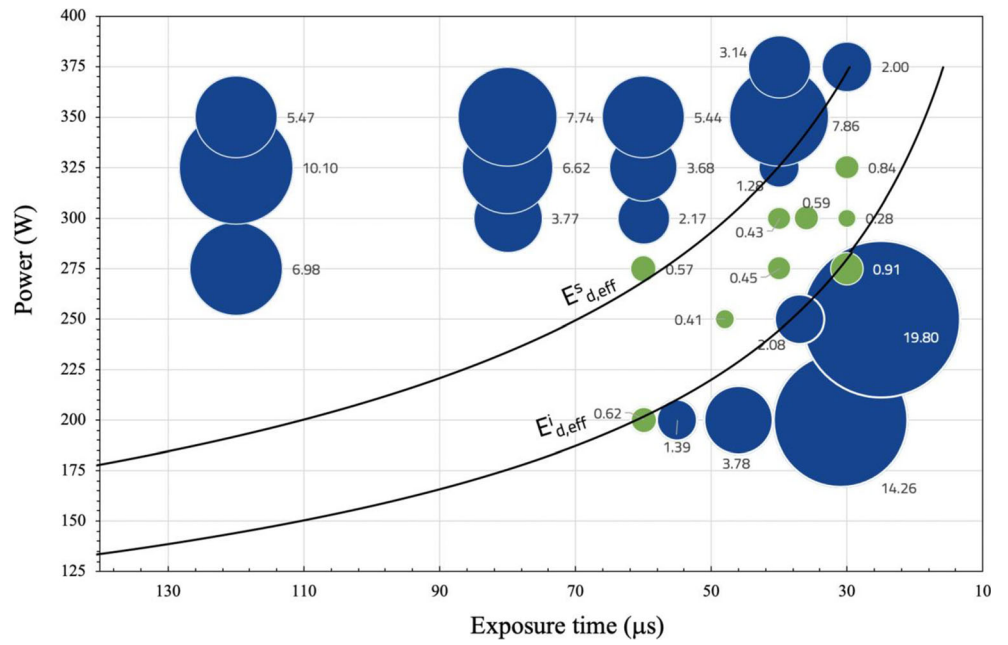
Fig. 10 Porosity versus VED: **a** original VED definition (Eq. (1)); **b** new VED definition (Eq. (6))

Fig. 11 SLM of Maraging steel 300. Porosity versus VED: **a** original VED definition (Eq. (1)); **b** new VED definition (Eq. (6)) (experimental data taken from [44])

fraction less than 1% (green bubbles in Fig. 9) with iso-VED curves obtained from the original formulation of the energy density (Eq. (1)). This is even demonstrated in Fig. 10 where the porosity versus VED is plotted. In Fig. 10a it is noted that there is no values of the E_d that promotes only low porosity containing specimens. On the contrary, by using the new definition of VED, $E_{d,\text{eff}}$, a narrow range of its values is obtained (3.2 J/mm^3 < $E_{d,\text{eff}}$ < 4.2 J/mm^3) that characterizes sound samples. This is attributed to the better capacity of the new definition of VED to capture the total energy absorbed by the powder bed. Therefore, all combinations of P and t_e that give a $E_{d,\text{eff}}$ value inside the 'safety' window shown in Fig. 10b will result in sound specimen. This is particularly useful when process parameters need to be selected in order to reduce the printing time without incurring to material defects. It is important to observe that the master diagram for process design shown in Fig. 9 may be used with caution because, first, it is obtained with fixed geometrical parameters and second, by

moving from cylindrical samples to industrial parts, the different geometries and sizes may influence the material soundness, as well. Despite this, $E_{d,\text{eff}}$ values can be used as guidelines to drastically reduce the setup of the industrial PBF process. Finally, it was observed that lack of fusion defects are promoted with $E_{d,\text{eff}}$ < 3.2 J/mm^3, while gas porosity is formed with $E_{d,\text{eff}}$ > 4.2 J/mm^3 (Fig. 10b).

In order to consolidate the use of the proposed modified VED as design parameter, it was chosen to apply it to experimental data taken from literature about SLM of Maraging steel 300 [44]. Results are shown in terms of porosity versus VED (Eq. (1)) (Fig. 11a) as well as porosity versus modified VED (Eq. 5) (Fig. 11b). It is clearly shown how the use of the proposed modified VED is able to discriminate a narrow range of energy density (as in previous case) in which sound specimens, characterized by the lowest porosity values, can be obtained. On the opposite, the use of standard VED

formulation is unable to explain or account for the differences in the observed process outcomes, as also outlined by the authors of the paper which experimental data are taken from [44].

It is worth noting that the proposed energy density equation works well even with different values of the layer thickness (d). However, it is not proved yet Eq. (5) is sensitive to other process parameters such as spot diameter, platform temperature, hatch distance, raster strategy, or building direction that in the present experiments were kept constant. Therefore, further experimental works are needed to establish the limits of the proposed relation.

5 Conclusions

The volumetric energy density is investigated as design process parameter starting from the assumption made in literature that samples obtained with the same value of energy density are characterized by the same amount of porosity. The original formulation of the volumetric energy density applied to the optimization of AlSi10Mg laser powder bed fusion process does not work, mainly because it does not quantify the actual energy absorbed by the powder.

In order to overcome drawbacks linked to the original formulation that does not consider the interaction between the heat source and the powder, a new expression is obtained and validated with experimental data, which shows that the energy density depends on the square root of the scan speed.

As a result, using the new expression of the volumetric energy density, it is found that all samples characterized by a porosity less than 1% fall in between a narrow range of its values. Moreover, the new VED formulation was used to predict the best process parameters (dealing with porosity) in SLM of Maraging steel 300, proving its extensibility to other kind of materials.

Therefore, provided that all the other variables such as spot diameter, platform temperature, hatch distance, raster strategy, and building direction are kept constant, the new formulation of the energy density can be used as design parameter to select the best combination power-scan speed.

Appendix

Table 2 Powers and exposure times used in experiments and resulting porosity (AlSi10Mg aluminium alloy)

Power (W)	Exposure time (t_e) (ms)	Porosity (%)
275	30	0.91
275	40	0.45
275	60	0.57
275	120	6.98
300	30	0.28
300	40	0.43
300	60	2.17
300	80	3.77
325	30	0.48
325	40	1.28
325	60	3.68
325	80	6.62
325	120	10.1
350	40	7.86
350	60	5.44
350	80	7.74
350	120	5.47
375	30	2.00
375	40	3.14
200	31	14.26
250	25	19.8
200	46	3.90
250	37	2.10
200	55	1.40
300	36	0.60
200	60	0.62
250	48	0.41

References

1. Razavi S, Bordonaro G, Ferro P, Torgersen J, Berto F (2018) Fatigue behavior of porous Ti-6Al-4V made by laser-engineered

net shaping. Materials (Basel) 11:284. https://doi.org/10.3390/ma11020284

2. Sames WJ, List FA, Pannala S, Dehoff RR, Babu SS (2016) The metallurgy and processing science of metal additive manufacturing. Int Mater Rev 61:315–360. https://doi.org/10.1080/09506608.2015.1116649

3. Razavi SMJ, Ferro P, Berto F, Torgersen J (2018) Fatigue strength of blunt V-notched specimens produced by selective laser melting of Ti-6Al-4V. Theor Appl Fract Mech 97:376–384. https://doi.org/10.1016/j.tafmec.2017.06.021

4. Razavi S-M-J, Ferro P, Berto F (2017) Fatigue assessment of Ti–6Al–4V circular notched specimens produced by selective laser melting. Metals (Basel) 7:291–301. https://doi.org/10.3390/met7080291

5. Bidare P, Maier RRJ, Beck RJ, Shephard JD, Moore AJ (2017) An open-architecture metal powder bed fusion system for in-situ process measurements. Addit Manuf 16:177–185. https://doi.org/10.1016/j.addma.2017.06.007

6. Everton SK, Hirsch M, Stravroulakis P, Leach RK, Clare AT (2016) Review of in-situ process monitoring and in-situ metrology for metal additive manufacturing. Mater Des 95:431–445. https://doi.org/10.1016/j.matdes.2016.01.099

7. Berumen S, Bechmann F, Lindner S, Kruth JP, Craeghs T (2010) Quality control of laser- and powder bed-based additive manufacturing (AM) technologies. Phys Procedia 5:617–622. https://doi.org/10.1016/j.phpro.2010.08.089

8. Holzmond O, Li X (2017) In situ real time defect detection of 3D printed parts. Addit Manuf 17:135–142. https://doi.org/10.1016/j.addma.2017.08.003

9. Schelmetic T (2018) GENOA 3DP additive manufacturing simulation tool updated to add metal AM. Des News

10. Bandyopadhyay A, Traxel KD (2018) Invited review article: Metal-additive manufacturing—Modeling strategies for application-optimized designs. Addit Manuf 22:758–774. https://doi.org/10.1016/j.addma.2018.06.024

11. Gong H, Rafi K, Gu H, Starr T, Stucker B (2014) Analysis of defect generation in Ti–6Al–4V parts made using powder bed fusion additive manufacturing processes. Addit Manuf 1–4:87–98. https://doi.org/10.1016/j.addma.2014.08.002

12. Nakamoto T, Shirakawa N, Miyata Y, Inui H (2009) Selective laser sintering of high carbon steel powders studied as a function of carbon content. J Mater Process Technol 209:5653–5660. https://doi.org/10.1016/j.jmatprotec.2009.05.022

13. Dilip JJS, Ram GDJ, Starr TL, Stucker B (2017) Selective laser melting of HY100 steel: process parameters, microstructure and mechanical properties. Addit Manuf 13:49–60. https://doi.org/10.1016/j.addma.2016.11.003

14. Simchi A (2006) Direct laser sintering of metal powders: mechanism, kinetics and microstructural features. Mater Sci Eng A 428:148–158. https://doi.org/10.1016/j.msea.2006.04.117

15. Simchi A, Pohl H (2003) Effects of laser sintering processing parameters on the microstructure and densification of iron powder. Mater Sci Eng A 359:119–128. https://doi.org/10.1016/S0921-5093(03)00341-1

16. Mazur M, Leary M, McMillan M, Elambasseril J, Brandt M (2016) SLM additive manufacture of H13 tool steel with conformal cooling and structural lattices. Rapid Prototyp J 22:504–518. https://doi.org/10.1108/RPJ-06-2014-0075

17. Yadroitsev I, Krakhmalev P, Yadroitsava I (2015) Hierarchical design principles of selective laser melting for high quality metallic objects. Addit Manuf 7:45–56. https://doi.org/10.1016/j.addma.2014.12.007

18. Prashanth KG, Scudino S, Maity T, Das J, Eckert J (2017) Is the energy density a reliable parameter for materials synthesis by selective laser melting? Mater Res Lett 5:386–390. https://doi.org/10.1080/21663831.2017.1299808

19. Yadroitsev I, Bertrand P, Smurov I (2009) Mechanical properties of samples fabricated by selective laser melting. In: 14èmes Assises Européennes du Prototypage & Fabrication Rapide. Paris

20. Garibaldi M, Ashcroft I, Simonelli M, Hague R (2016) Metallurgy of high-silicon steel parts produced using selective laser melting. Acta Mater 110:207–216. https://doi.org/10.1016/j.actamat.2016.03.037

21. Scipioni Bertoli U, Wolfer AJ, Matthews MJ, Delplanque JPR, Schoenung JM (2017) On the limitations of volumetric energy density as a design parameter for selective laser melting. Mater Des 113:331–340. https://doi.org/10.1016/j.matdes.2016.10.037

22. Willy HJ, Li X, Chen Z, Herng TS, Chang S, Ong CYA, Li C, Ding J (2018) Model of laser energy absorption adjusted to optical measurements with effective use in finite element simulation of selective laser melting. Mater Des 157:24–34. https://doi.org/10.1016/j.matdes.2018.07.029

23. Cherry JA, Davies HM, Mehmood S, Lavery NP, Brown SGR, Sienz J (2015) Investigation into the effect of process parameters on microstructural and physical properties of 316L stainless steel parts by selective laser melting. Int J Adv Manuf Technol 76:869–879. https://doi.org/10.1007/s00170-014-6297-2

24. Ciurana J, Hernandez L, Delgado J (2013) Energy density analysis on single tracks formed by selective laser melting with CoCrMo powder material. Int J Adv Manuf Technol 68:1103–1110. https://doi.org/10.1007/s00170-013-4902-4

25. Taheri Andani M, Dehghani R, Karamooz-Ravari MR, Mirzaeifar R, Ni J (2017) Spatter formation in selective laser melting process using multi-laser technology. Mater Des 131:460–469. https://doi.org/10.1016/j.matdes.2017.06.040

26. Caiazzo F, Alfieri V, Casalino G (2020) On the relevance of volumetric energy density in the investigation of Inconel 718 laser powder bed fusion. Materials (Basel) 13:538. https://doi.org/10.3390/ma13030538

27. Hann DB, Iammi J, Folkes J (2011) A simple methodology for predicting laser-weld properties from material and laser parameters. J Phys D Appl Phys 44:445401. https://doi.org/10.1088/0022-3727/44/44/445401

28. Metelkova J, Kinds Y, Kempen K, de Formanoir C, Witvrouw A, van Hooreweder B (2018) On the influence of laser defocusing in selective laser melting of 316L. Addit Manuf 23:161–169. https://doi.org/10.1016/j.addma.2018.08.006

29. King WE, Barth HD, Castillo VM, Gallegos GF, Gibbs JW, Hahn DE, Kamath C, Rubenchik AM (2014) Observation of keyhole-mode laser melting in laser powder-bed fusion additive manufacturing. J Mater Process Technol 214:2915–2925. https://doi.org/10.1016/j.jmatprotec.2014.06.005

30. Soylemez E (2020) High deposition rate approach of selective laser melting through defocused single bead experiments and thermal finite element analysis for Ti-6Al-4V. Addit Manuf 31:100984. https://doi.org/10.1016/j.addma.2019.100984

31. Carter LN, Wang X, Read N et al (2016) Process optimisation of selective laser melting using energy density model for nickel based superalloys. Mater Sci Technol:1–5. https://doi.org/10.1179/1743284715Y.0000000108

32. Steen WM, Mazumder J (2010) Theory, mathematical modelling and simulation. In: Laser Material Processing. Springer London, London, pp 251–294

33. Incropera FP, DeWitt DP (2001) Fundamentals of heat and mass transfer, 5th edn. Wiley

34. van Elsen M, Al-Bender F, Kruth J (2008) Application of dimensional analysis to selective laser melting. Rapid Prototyp J 14:15–22. https://doi.org/10.1108/13552540810841526

35. Trapp J, Rubenchik AM, Guss G, Matthews MJ (2017) In situ absorptivity measurements of metallic powders during laser powder-bed fusion additive manufacturing. Appl Mater Today 9:341–349. https://doi.org/10.1016/j.apmt.2017.08.006

36. Guo Q, Zhao C, Qu M, Xiong L, Escano LI, Hojjatzadeh SMH, Parab ND, Fezzaa K, Everhart W, Sun T, Chen L (2019) In-situ characterization and quantification of melt pool variation under constant input energy density in laser powder bed fusion additive manufacturing process. Addit Manuf 28:600–609. https://doi.org/10.1016/j.addma.2019.04.021

37. Ning J, Sievers D, Garmestani H, Liang S (2019) Analytical modeling of in-process temperature in powder bed additive manufacturing considering laser power absorption, latent heat, scanning strategy, and powder packing. Materials (Basel) 12:808. https://doi.org/10.3390/ma12050808

38. Criales LE, Arısoy YM, Özel T (2016) Sensitivity analysis of material and process parameters in finite element modeling of selective laser melting of Inconel 625. Int J Adv Manuf Technol 86:2653–2666. https://doi.org/10.1007/s00170-015-8329-y

39. Liu B, Li B-Q, Li Z, Bai P, Wang Y, Kuai Z (2019) Numerical investigation on heat transfer of multi-laser processing during selective laser melting of AlSi10Mg. Results Phys 12:454–459. https://doi.org/10.1016/j.rinp.2018.11.075

40. Stacy SC, Zhang X, Pantoya M, Weeks B (2014) The effects of density on thermal conductivity and absorption coefficient for consolidated aluminum nanoparticles. Int J Heat Mass Transf 73:595–599. https://doi.org/10.1016/j.ijheatmasstransfer.2014.02.050

41. Gusarov AV (2010) Radiation transfer in metallic-powder beds during laser forming. Quantum Electron 40:451–459. https://doi.org/10.1070/QE2010v040n05ABEH013976

42. Yuri C (2011) Investigations of light transfer in powder bed. Phys Procedia 12:279–284. https://doi.org/10.1016/j.phpro.2011.03.036

43. Yang Y, Gu D, Dai D, Ma C (2018) Laser energy absorption behavior of powder particles using ray tracing method during selective laser melting additive manufacturing of aluminum alloy. Mater Des 143:12–19. https://doi.org/10.1016/j.matdes.2018.01.043

44. Mugwagwa L, Yadroitsev I, Matope S (2019) Effect of process parameters on residual stresses, distortions, and porosity in selective laser melting of maraging steel 300. Metals 9:1042–1057. https://doi.org/10.3390/met9101042